FREQUENCY-RECONFIGURABLE COLLOIDAL DISPERSION-BASED FILTERING DEVICES

An Undergraduate Research Scholars Thesis

by

AMANDA MARIE COUCH

Submitted to Honors and Undergraduate Research
Texas A&M University
in partial fulfillment of the requirements for the designation as

UNDERGRADUATE RESEARCH SCHOLAR

Approved by
Research Advisor: Dr. Gregory H. Huff

May 2014

Major: Electrical Engineering

TABLE OF CONTENTS

ABSTRACT

Frequency-reconfigurable Colloidal Dispersion-based Filtering Devices. (May 2014)

Amanda Marie Couch
Department of Electrical and Computer Engineering
Texas A&M University

Research Advisor: Dr. Gregory H. Huff
Department of Electrical and Computer Engineering

Many electronics today are susceptible to harm caused by high power transient waveforms. To protect electronic devices and systems from high power transient waveforms, shielding or some form of electronic hardening is required. A potential method for protecting electronic devices and systems from high power transient waveforms is the use of colloidal microstructures. Recent experiments done characterizing the AC electrical properties of colloidal dispersions show that the geometry of the colloids in the microstructure can be manipulated by frequency. This project intends to use colloidal dispersions to create frequency reconfigurable transmission line structures. The frequency reconfigurable structures, based on a coaxial line and a coplanar waveguide, will be simulated in HFSS and fabricated in Texas A&M Electromagnetics and Microwaves Laboratories. Microscopy will be used to monitor the motion of the particles within the transmission line structures, and the small signal parameters of the structures will be measured using a network analyzer. The end result of the project will be an equivalent circuit model per unit length that characterizes the colloidal dispersion-based transmission line structure.

ACKNOWLEDGMENTS

I would like to thank Dr. Huff for his assistance, guidance, and mentorship both on this project and over the past four years. In addition, I would like to thank Nick Brennan for all of his help with this project and every other project about which I've pestered him with questions. I would also would like to acknowledge our colleagues at Johns Hopkins and the NRL for all of the great work they do on this project.

NOMENCLATURE

AC	Alternating Current
CPW	Coplanar Waveguide
CPWG	Coplanar Waveguide with Ground
EML	Electromagnetic and Microwaves Laboratories
EMP	Electromagnetic Pulse
HPTW	High Power Transient Waveform
RF	Radio Frequency

CHAPTER I

INTRODUCTION

High power transient waveforms, which can be caused by a high altitude EMP [6] or AC to DC power converter and naturally occur in space [8], are a threat to damage many electronic devices. Particularly, in systems incorporating a switched-mode power supply, often used for its efficient conversion of AC to DC power, transient waveforms are a serious concern [5]. In addition, as technology incorporates low-power, low-voltage transistors, electronics become more susceptible to damage and corruption caused by transient waveforms. Transient waveforms create single-event transients, such as single event latchup (SEL), single event gate rupture (SEGR), and single event upset (SEU). SEL and SEGR can damage low voltage electronics, while SEU causes data corruption. To protect electronic devices from damage due to high power transient voltages, methods are needed to shield the electronic devices from the waveforms.

Currently proposed methods of mitigating the threat of damage from high power transient waveforms are placing Faraday cages around the electronic equipment or incorporating an on-board shielding structure incorporating a low pressure gas above a frequency selective substrate [4]. When Faraday cages or the use of a low pressure gas is impractical, other solutions to the potential of high power transient waveforms are needed.

High Power Transient Waveforms

For the purposes of this work, high power transient waveforms will be modeled by the standards for a high-altitude EMP set in [2] . This standard models the high altitude EMP as a difference of two exponentials. The basic equation for the waveform is:

$$e^{-\beta t} - e^{-\alpha t} \tag{I.1}$$

where β determines the rise of the waveform and α determines the fall of the waveform. The time domain waveform is shown in Fig. I.1. Further characteristics defined by the standards

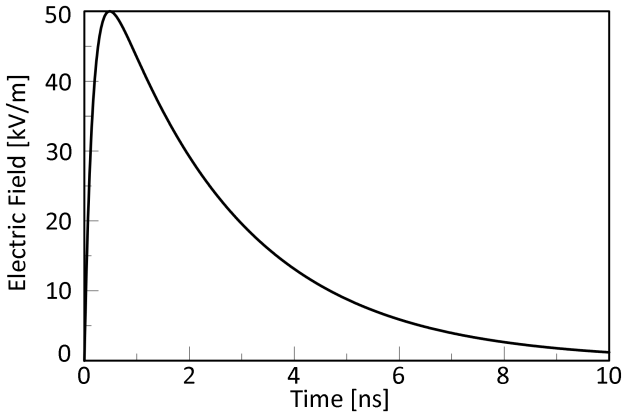

Fig. I.1. Time domain waveform as defined in [2]

include a peak electric field value of 50 kV/m and a peak spectrum width of 18.8 MHz. The full spectrum expands beyond 100 MHz. Fig. I.2 displays the full spectrum of the modeled waveform.

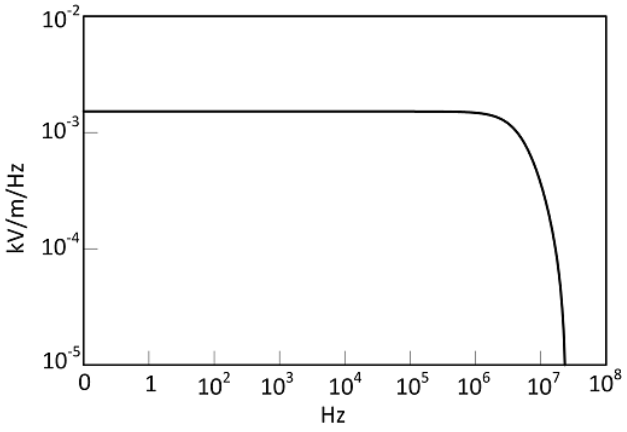

Fig. I.2. Frequency spectrum for a high altitude EMP as defined in [2]

Colloidal Microstructures and Colloidal Dispersion

Recently, the AC electrical properties of colloidal microstructures have been examined and show that the arrangement of the colloids present in the microstructure can be controlled by frequency. Specifically, when an electric field with a certain frequency is applied to the microstructure, the colloids form chains that short (direct the incoming waveform to ground) the microstructure [1]. These colloidal microstructures provide a new potential method for protecting electronic devices against high power transient waveforms. Since the colloidal microstructures form chains when frequencies above a certain threshold are applied, the colloidal microstructure can be used to develop low-pass filters or switch-like components that protect electronic devices from high power transient waveforms.

Conductive Particles

A type of particle used in colloidal microstructures is conductive particles such as gold, aluminum, or copper. With these particles, as the frequency of the waveform changes, the arrangement of the particles shifts. Fig. I.3 displays 800nm gold particles forming chains as a function of frequency. When low frequencies are applied to the microstructures containing the conductive particles, the main transport method of the particles is electrophoresis. Electrophoresis can be clearly seen occuring at in the first column of Fig. I.3. As the frequency is increased, the transport method the particles shifts from electrophoresis to dielectrophoresis. In dielectrophoresis, the applied waveform induces dipole moments within the individual particles, creating the chain-like geometry of the particles appearing at the higher voltages and higher frequencies.

Dielectric Particles

Dielectric particles within a structure have been shown to be used for the frequency tuning of a structure through manipulating dielectric properties, specifically the effective dielectric constant, of a material. The effective dielectric constant ϵ_{eff} for mixing spherical particles of

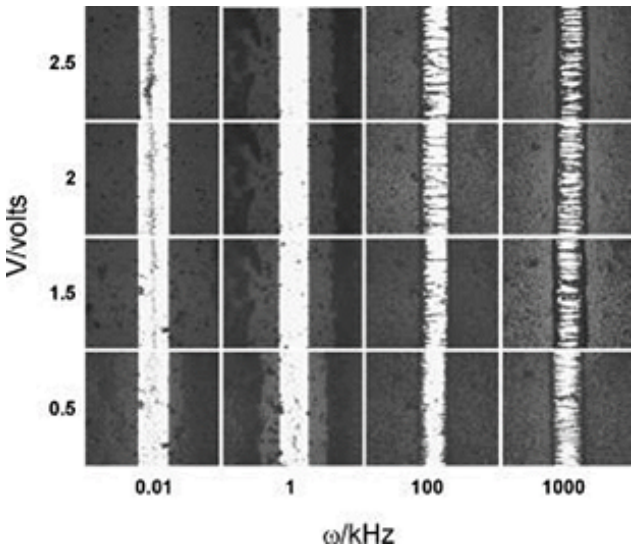

Fig. I.3. Particle arrangement changing as a result of frequency. Picture taken from [1]

dielectric constant ϵ_1 with a medium of dielectric constant ϵ_m is determined by the Maxwell-Garnet Mixing Rule [7]. The mixing rule is as shown:

$$\frac{\epsilon_{eff} - \epsilon_m}{\epsilon_{eff} + 2\epsilon} = f\frac{\epsilon_1 - \epsilon_m}{\epsilon_1 + 2\epsilon_m} \tag{I.2}$$

where f is the volume fraction of the spherical particles. This formula can be also applied to conductive particle by using the complex form dielectric constant where:

$$\epsilon_{compl} = \epsilon - \frac{\jmath\sigma}{\omega} \tag{I.3}$$

For a particle with a dielectric constant ϵ_1 and a dielectric shell of ϵ_2 mixed within a medium with dielectric constant ϵ_m the effective dielectric constant ϵ_{eff} becomes:

$$\frac{\epsilon_{eff} - \epsilon_m}{\epsilon_{eff} + 2\epsilon} = f_1\frac{\epsilon_1 - \epsilon_m}{\epsilon_1 + 2\epsilon_m} + f_2\frac{\epsilon_2 - \epsilon_m}{\epsilon_2 + 2\epsilon_m} \tag{I.4}$$

where f_1 is the volume fraction of the spherical particles, without the dielectric shell, and f_2 is the volume fraction of the shell alone. Both cases of the Maxwell-Garnet Mixing rule will be examined further with respect to particle size and shell thickness in chapter III.

Transmission Lines

Transmission lines are structures designed to allow currents with RF content to propagate through the structure. The two types of transmission lines used in this project will be coaxial cable and coplanar waveguide with ground (CPWG) structures. Coaxial cable contains three main components: a center metal core, a dielectric layer, and a metal cladding layer. CPWG lines are created by etching or milling two parallel lines into the copper layer atop a dielectric substrate with a ground layer. Fig. I.4 displays cross sections of both coaxial and CPWG structures.

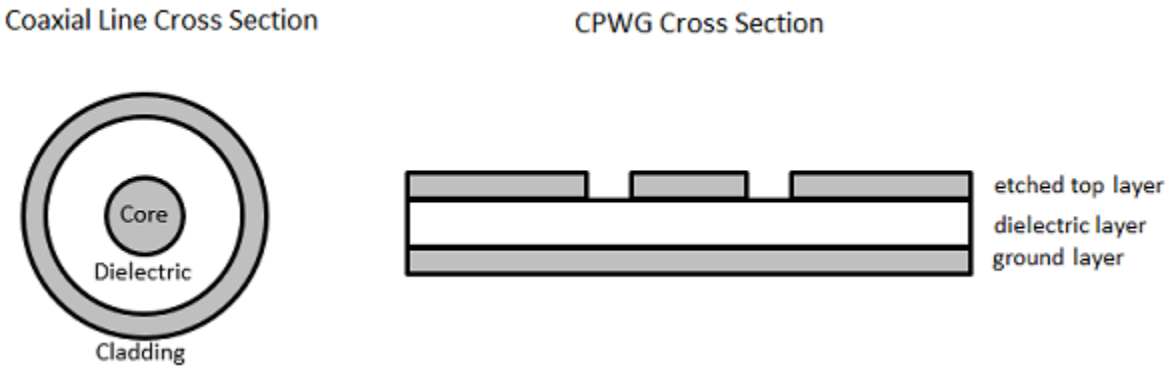

Fig. I.4. Cross sections of different types of transmission line

Regardless of structure, all transmission lines can be generically modeled as series inductor and resistor with a parallel capacitor and resistor [3]. Considering a differential section of

transmission line length Δx located at point x at time t, the voltage and current can be defined as:

$$v(x+\Delta x,t)-v(x,t)=\Delta v(x,t)i(x+\Delta x,t)-i(x,t)=\Delta i(x,t) \tag{I.5}$$

Now, we define the resistance of the series resistor and inductor as R and L, and we define the shunt capacitance and conductance as C and G, respectively and in relation to the differential length of transmission line. Then,

$$\Delta v(x,t)=-(R\Delta x)i(x,t)-(L\Delta x)\frac{\partial i(x,t)}{\partial t} \tag{I.6}$$

$$\Delta i(x,t)=-(G\Delta x)v(x+\Delta x,t)-(C\Delta x)\frac{\partial v(x+\Delta x,t)}{\partial t} \tag{I.7}$$

After dividing by Δx we find the well known Telegrapher's Equations [3]:

$$\frac{\partial v(x,t)}{\partial x}=-R(i(x,t))-L\frac{\partial i(x,t)}{\partial t} \tag{I.8}$$

$$\frac{\partial i(x,t)}{\partial x}=-G(v(x,t))-C\frac{\partial v(x,t)}{\partial t} \tag{I.9}$$

And now differentiating with respect to x leaves us with two coupled differential equations shown below:

$$\frac{\partial^2 v(x,t)}{\partial x}=-R\frac{\partial i(x,t)}{\partial t}-L\frac{\partial^2 i(x,t)}{\partial t^2} \tag{I.10}$$

$$\frac{\partial^2 i(x,t)}{\partial x}=-G\frac{\partial v(x,t)}{\partial t}-C\frac{\partial^2 v(x,t)}{\partial t^2} \tag{I.11}$$

Assuming a steady-state case, one can switch to phasor notation. This allows us to combine the two equations I.10 and I.11 into one equation:

$$\frac{d^2V(x)}{dx^2}-\sqrt{(R+j\omega L)(G+j\omega C)}V(x)=0 \tag{I.12}$$

Equation I.12 is the wave equation with a propagation constant γ of $\sqrt{(R+j\omega L)(G+j\omega C)}$. From this solution, we can determine the characteristic impedance of a line Z_0 as:

$$Z_0 = \sqrt{\frac{R+j(2\pi f)L}{G+j(2\pi f)C}} \tag{I.13}$$

Given $\omega = 2\pi f$, equation I.13 can be rewritten as:

$$f = \frac{GZ_0^2 - R}{2\pi j(L - CZ_0^2)} \tag{I.14}$$

The solution to the Telegraph's Equations allows one to calculate several important properties of transmission lines from characteristic impedance and propagation constant such as reflection coefficient, input impedance, and voltage standing wave ratio (VSWR).

By incorporating different dispersions with a variety of particle sizes and types, we will be able to design components that manipulate the resistance, inductance, conductance, and capacitance of its system. Given a particular characteristic impedance of the system, the variation in R,L,G, and C allow for the variation of the frequency of the system. This modeling of a section of transmission line as a $R-L-G-C$ circuit will be further explored in the discussion of an equivalent circuit model in chapter IV.

CHAPTER II

METHODOLOGY

In order to examine the use of colloidal microstructures in electronic systems, we developed filtering devices based on two different types of transmission line structures. The first structure designed was based on a section of coaxial line while the second structure was based on a coplanar waveguide with ground (CPWG) line. Dispersions with varying colloidal particle sizes and particle shapes were be placed in the transmission line structures. The dispersions used in [1] will be the focus of the work in this project.

Simulation of Transmission Line Structures

The transmission line structures containing the colloidal dispersions were designed and analyzed in the electromagnetics simulation software High Frequency Simulation Software (HFSS). All simulations were ran at frequencies varying from 100kHz to 5GHz. The first transmission structures analyzed were based off a cross-section of a coaxial cable. The first structure analyzed was a cross section of a 50 Ω coaxial cable with four rectangular arms ranging from the outer conductor towards the inner conductor. A 10μm gap of variable conductivity, which models the conductive particles, was placed between each arm and the inner conductor. The conductivity with this gap was varied between 0 and 10^6 S/m. Fig. II.1 displays the simulated 4-arm structure with 10μm gap. The other transmisssion line structure explored was a CPWG-based structure. The first structure simulated, displayed in Fig. II.2 was a 50 Ω CPWG structure with inserts placed atop the substrate at the midpoint of the structure. The inserts began at the outer planes of the CPWG line and extended towards the center line, allowing for a 10μm gap where the conductive particles were located. Like with the coaxial line structure, the conductivity within the gap for the CPWG structure was varied between 0 and 10^6 S/m.

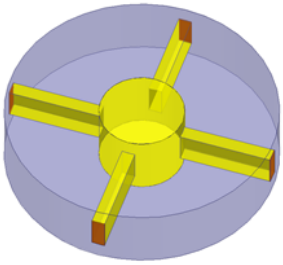

Fig. II.1. Example of a coaxial based filtering device

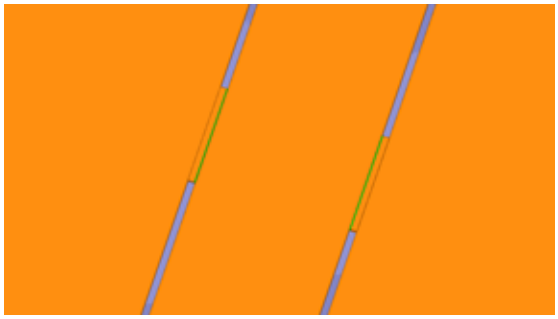

Fig. II.2. Example of a CPWG based filtering device

Fabrication of Transmission Line Structures

Several of the designs analyzed were fabricated at Johns Hopkins using photolithography. The motion and geometry of the particles were examined using microscopy and a signal generator, and the S-parameters of the structures were measured using a network analyzer. The size and shape of the particles present within the microstructure gaps were varied to examine the relationship between frequency and the type of particle. The results of these tests will be discussed in chapter III

In addition, a select few designs previously simulated in a coaxial cable or on 62 mil Duriod 5880 substrate were redesigned to use a 1mm glass substrate. The coaxial cable iterations were resimulated in HFSS as a CPWG fed planar structure. Fig. II.3 displays an example of one of the redesigned coaxial line structures. The new designs were etched onto a glass slide by Photo Sciences, inc. Like with the designs fabricated at Johns Hopkins, the S-parameters of the structures were measured and the motion of the particles was recorded. The results of these tests will also be discussed in chapter III.

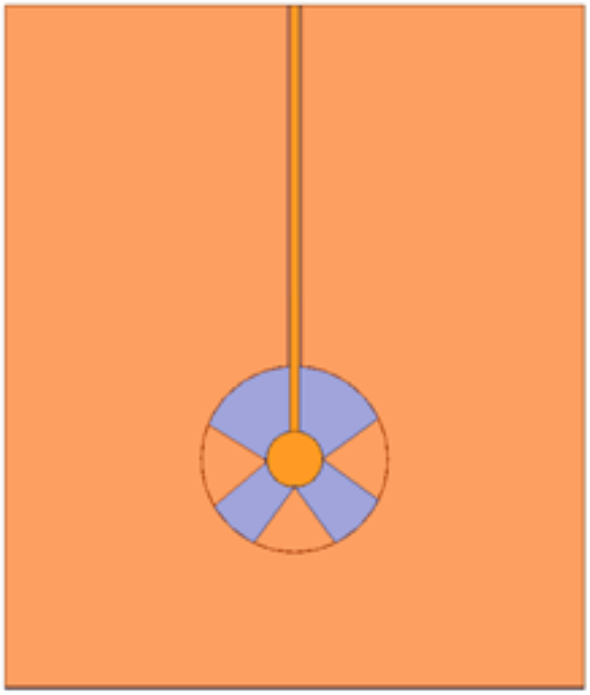

Fig. II.3. A CPWG fed coaxial line test structure simualted on 1mm glass substrate

CHAPTER III

RESULTS

In this chapter, the results from the HFSS simulations and device testing are presented. The HFSS results will be further examined in chapter IV in the discussion on the development of equivalent circuit models for each transmission line structure.

Simulation of the Coaxial Filtering Devices

The filtering devices developed were based on two different types of transmission line structures, coaxial line and coplanar waveguide with ground (CPWG). The coax-based designs use standard SMA coax dimensions and contain the same particle gap width of 10μm. Fig. III.1 displays the first iteration of the coax-based structure. The structure uses four rectangular arms spanning from the inner conductor to the outer conductor and includes 10μm gaps between each arm and the outer conductor. The arms of the structure are .5mm tall and .2 mm wide. The second iteration, shown in Fig. III.2, places the gap between the arm and the inner conductor.

Due to the strength of the electric fields of a coaxial structure at the center conductor, we moved the colloidal microstructures at the inner gap. As shown in III.3 and III.4, the move maintained the same levels of attenuation, while providing the opportunity to reduce the cases $\sigma = 0$ and $\sigma = 1$ insertion loss in future iterations. Low $\sigma = 0$ and $\sigma = 1$ insertion loss allow for minimal degradation or attenuation of RF signal when the filtering device is inactive. The max attenuation for both iterations was greater then 40dB.

Fig. III.5 replaced the rectangular arms cones with spherical tips to reduce the insertion loss present in the rectangular arm structures when the gap was in a low conductivity state, while also increasing the signal attenuation when the gap was in a high conductivity state. Like the second iteration, the third iteration placed the particle gaps between the end of the arm and the inner conductor. The fourth iteration, shown in Fig. III.6, increased the

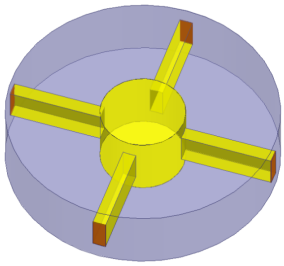

Fig. III.1. Four rectangular arm structure with gap at outer conductor

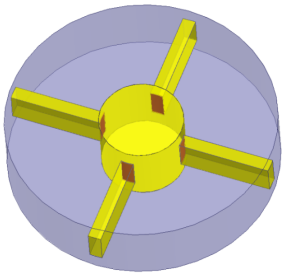

Fig. III.2. Four rectangular arm structure with gap at inner conductor

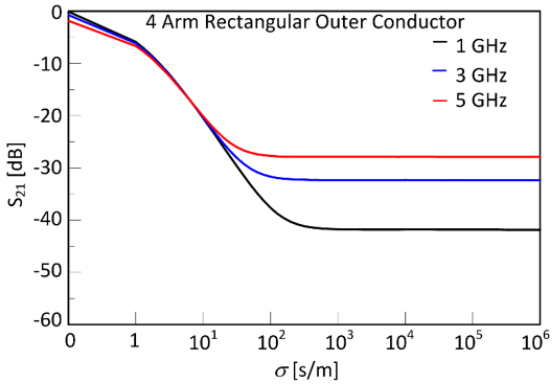

Fig. III.3. Results for four arm outer rectangular structure

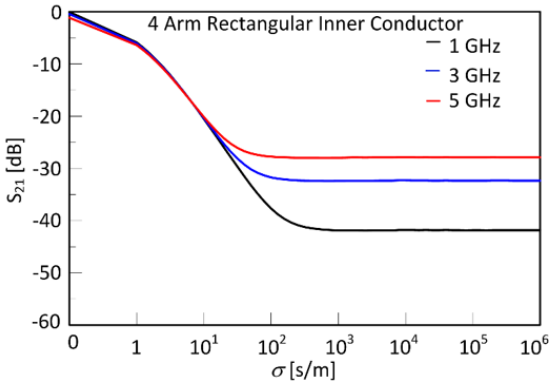

Fig. III.4. Results for four arm inner rectangular structure

number of conical arms from four to six in order to further increase the signal attenuation without compromising the insertion loss. Fig. III.7 and Fig. III.8 show how the attenuation of each structure increases with σ. In particular, these conical structures have low insertion loss at $\sigma = 0$ and $\sigma = 1$. The six conical arm structure allows about 50dB of attenuation at 1GHz, as shown in Fig. III.8.

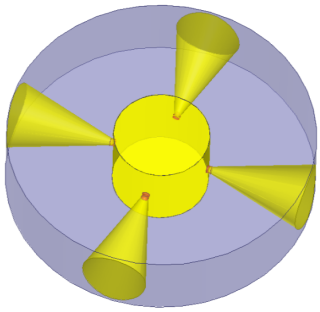

Fig. III.5. Four conical arm structure

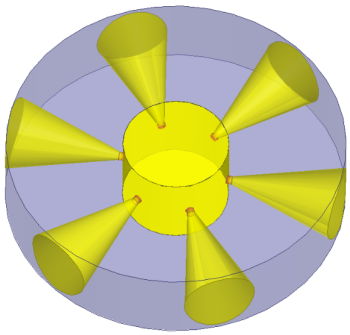

Fig. III.6. Six conical arm structure

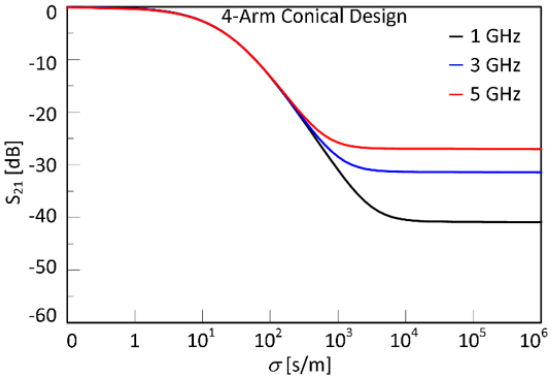

Fig. III.7. Four arm conical results

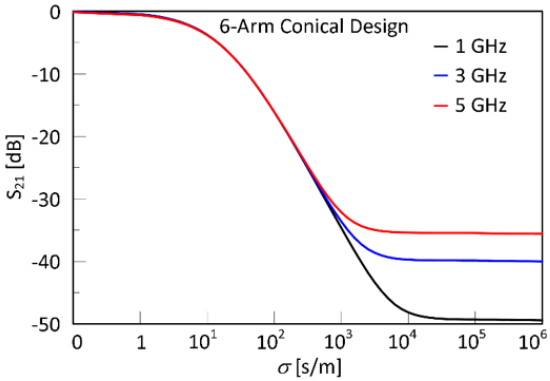

Fig. III.8. Six arm conical results

Simulation of the CPWG-based Filtering Devices

The CPWG-based structures contain inserts placed atop the substrate at the midpoint of the structure. The inserts begin at the outer planes of the CPWG line and extend towards the center line, allowing for a 10um gap where the conductive particles are located. Two versions

of the CPWG-based structures were simulated, one with rectangular inserts and another with arced inserts, displayed in Fig. III.9 and Fig. III.10 respectively. Both CPWG-based structures produced greater signal attenuation when the gaps were in a high conductivity state compared to the coax-based structures. The rectangular insert structure produced the greatest amount of attenuation of all simulated structures, allowing for a max attenuation of almost 60dB.

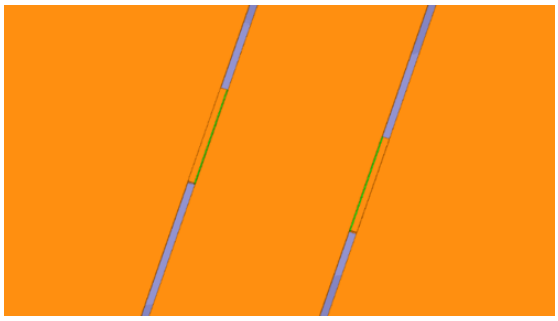

Fig. III.9. CPWG-based filtering structure with rectangular inserts

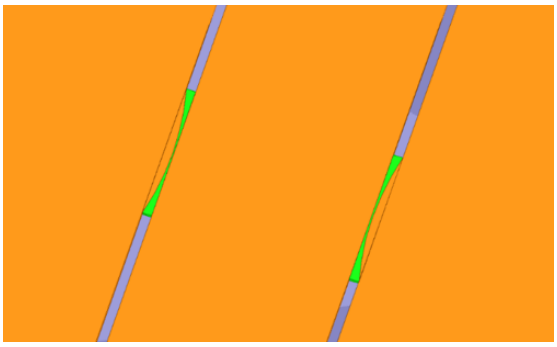

Fig. III.10. CPWG-based filtering structures with arc-shaped inserts

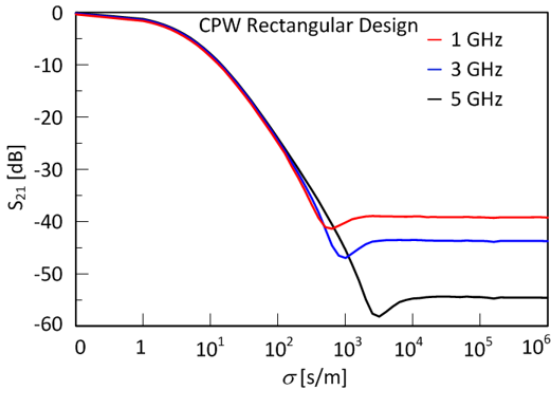

Fig. III.11. CPWG-based filtering structure with rectangular inserts results

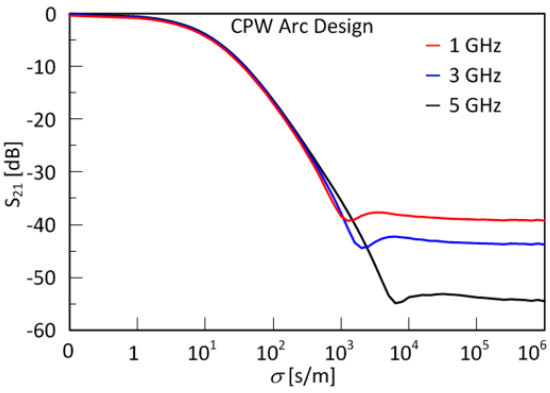

Fig. III.12. CPWG-based filtering structure with arc-shaped inserts results

Out of the four structures, the two structures that will be further examined are the six arm coaxial structure and the CPWG-based structure with rectangular inserts. The six arm

coaxial structure produced both high active signal attenuation and low inactive insertion loss. The CPWG structure with rectangular inserts will be further examined due to the structure achieving the highest attenuation of the structures explored. Fig. III.13 compares the signal attenuation versus σ across all structures at 3dB.

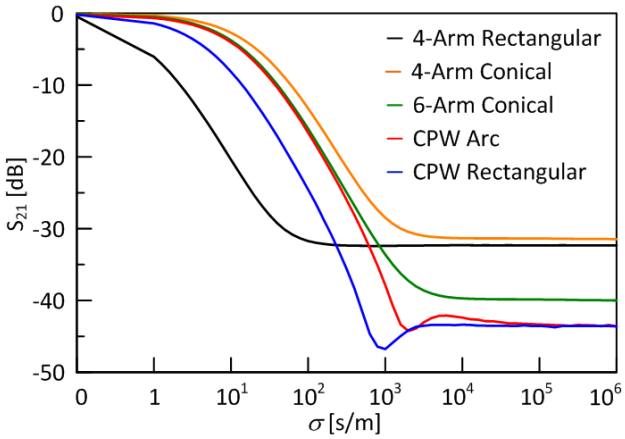

Fig. III.13. Comparison of all structures

Testing of the Coaxial Filtering Devices

Our colleagues at Johns Hopkins have fabricated and tested the operation of the planar versions of the coax-based structures. Fig. III.14 and Fig. III.15 display the shift in transport method from electrophoresis to dielectrophoresis as the voltage applied to the structure increases from 0V to 5V. These results demonstrate the basic filtering and switching mechanism working within a planar coaxial structure.

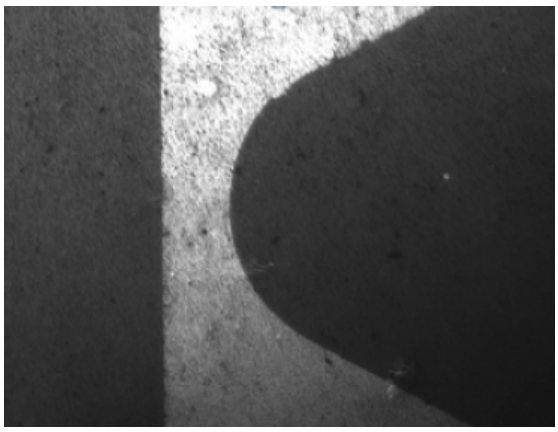

Fig. III.14. Colloid geometry at 0V

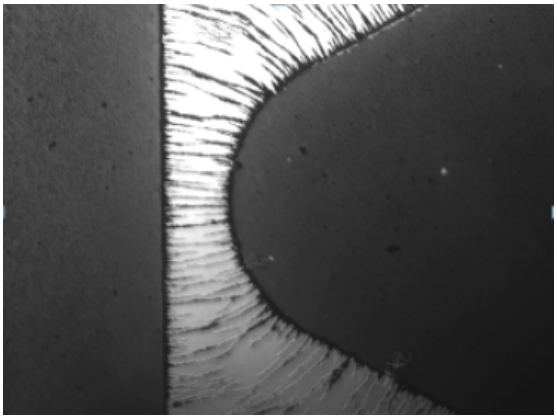

Fig. III.15. Colloid geometry at 5V

CHAPTER IV

DISCUSSION

From the simulated results shown in Fig. III, we derived an equivalent circuit model for the transmission line structures. The method below outlines the procedure for deriving models for both structures.

Step 1: Divide transmission line structure into N slices

Step 2: Calculate γ and Z_0 for each of these structures, where Z_0 is the intrinsic impedance of the line and γ is the complex propagation constant defined as:

$$\gamma = \alpha + \jmath\beta \tag{IV.1}$$

Step 3: From Z_0 and γ, calculate the ABCD matrices for a section of transmission line length l, which is the length of the slice. ABCD matrices in general are defined as:

$$\begin{vmatrix} A & B \\ C & D \end{vmatrix} = \begin{vmatrix} \frac{V_2}{V_1}|_{I_1=0} & \frac{V_2}{I_1}|_{V_1=0} \\ -\frac{I_2}{V_1}|_{I_1=0} & -\frac{I_2}{I_1}|_{V_1=0} \end{vmatrix} \tag{IV.2}$$

Any section of transmission line length l has the ABCD matrix defined as:

$$\begin{vmatrix} \cosh(\gamma l) & Z_0 \sinh(\gamma l) \\ \frac{1}{Z_0}\sinh(\gamma l) & \cosh(\gamma l) \end{vmatrix} \tag{IV.3}$$

Step 4: Find the ABCD matrix for the slice equivalent topology. For example, if the slice is equal to a series L and shunt C, the matrix would be:

$$\begin{vmatrix} 1 + S^2LC & sL \\ sC & 1 \end{vmatrix} \tag{IV.4}$$

Step 5: Set the matrices from 3 and 4 equal and solve for the values of the equivalent circuit.

Step 6: From the values for the lumped elements of the equivalent circuit, calculate new Z_0 and γ.

Step 7: From new Z_0 and γ, calculate the equivalent ABCD matrices for each sliced section.

Step 8: Multiply the ABCD matrices for each slice to find an ABCD matrix that approximates the entire structure

Step 9: Convert the ABCD matrix to S-parameters and compare to the HFSS results.

Coax Model

First, we divided the transmission line structure into 30 slices. For a visual representation of the slicing, Fig. IV.1 displays the a design divided into 5 slices. From the six arm conical structure discussed in chapter III, we calculated Z_0 and γ for each sliced approximation. We then calculated the ABCD matrix as shown in equation IV.3 above. For any lossless portion of transmission line, or a region without particles, we modeled the slice as an L-C circuit, shown in Fig. IV.2. Due to nature of a lossless transmission line, equation IV.3 above transforms to

$$\begin{vmatrix} \cos(\beta l) & \jmath \sin(\beta l) \\ \jmath \frac{1}{Z_0} \sin(\beta l) & \cos(\beta l) \end{vmatrix} \tag{IV.5}$$

By equating IV.4 and IV.5, we calculated L_a and C_a as follows:

$$\frac{\jmath \sin(\beta l)}{s} = L_a \tag{IV.6}$$

$$\frac{\jmath \frac{1}{Z_0} \sin(\beta l)}{s} = C_a$$

By repeating this process for every slice within the coaxial line, we found C and L as functions of length within the coaxial line as shown in Fig. IV.3 and Fig. IV.4. Now that we found L and C as a function of location within the transmission line structure, we solved for the particle containing portions, or lossy slices, of the coaxial design. We modeled these

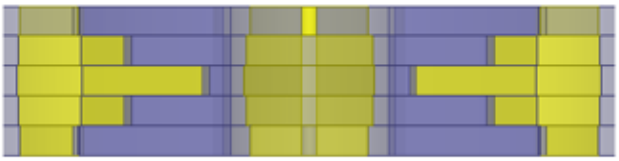

Fig. IV.1. Visual representation for sliced approximation of the coax model

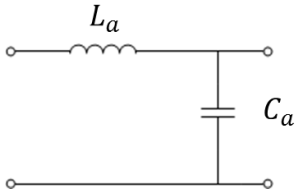

Fig. IV.2. Series L and shunt C circuit for modeling a loseless section transmission line

sections as $L - R - C$ networks as shown in Fig. IV.5. The L and C in this network were found while calculating the lossless portion of transmission line. Using the definition of an ABCD matrix, we found R_b from equation IV.7.

$$Z_0 \sinh(\gamma l) = \jmath\omega L_a \tag{IV.7}$$

$$\frac{1}{Z_0} \sinh(\gamma l) = R_a + \jmath\omega C_a$$

Since the location of the particles was fixed, we calculated a curve for R in relation to σ. Fig. IV.6 displays how R changes as a function of σ. As anticipated, R is low when σ is low and R increases approximately linearly with σ. From these functions for L, C and R, we calculated a new Z_0 and γ for each slice. For the lossless cases:

$$Z_0 = \sqrt{\frac{L_a}{C_a}} \tag{IV.8}$$

$$\beta = \omega\sqrt{L_a C_a}$$

and for the lossy cases:

$$Z_0 = \sqrt{\frac{\jmath L_a}{R_b + \jmath C_a}} \tag{IV.9}$$

$$\beta = \omega\sqrt{(\jmath\omega L_a)(R_b + \jmath\omega C_a)}$$

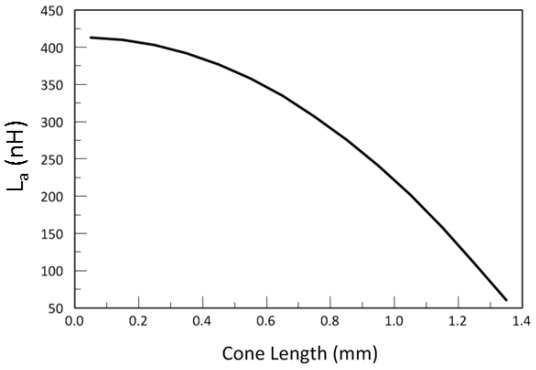

Fig. IV.3. L_a as a function of cone insertion into coax line

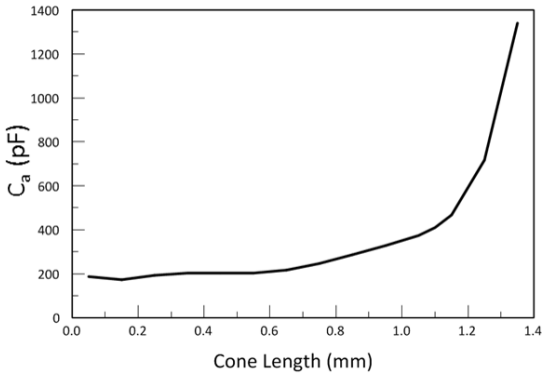

Fig. IV.4. C_a as a function of cone insertion into coax line

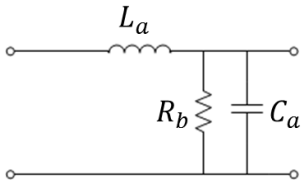

Fig. IV.5. Circuit for modeling a lossy section of transmission line

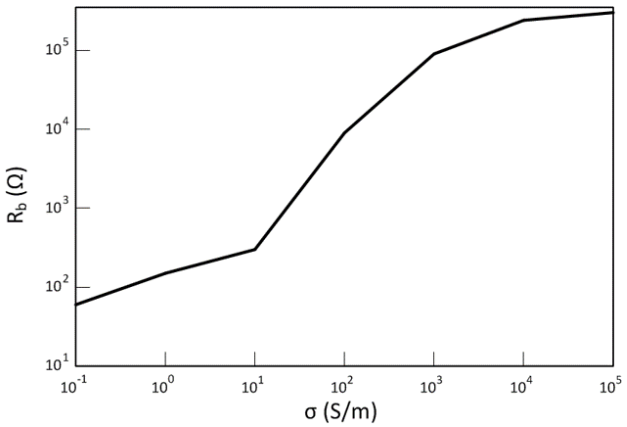

Fig. IV.6. R_b as a function gap conductivity

From these terms, we then calculated new ABCD matrices for each slice and multiplied all of these matrices together to find one ABCD matrix to represent the entire structure. We then converted the ABCD matrix into a set of S-parameters. By repeating this process for all expected values of σ, we were able to calculate the S-parameters for a lumped element network and compare it to my simulated HFSS data. Fig. IV.8, Fig. IV.9, Fig. IV.10, and Fig. IV.11 compare the equivalent circuit model to the simulated results. The equivalent circuit model results closely follow the simulated results, verifying that the equivalent circuit model appropriately characterizes the simulated coaxial line structure.

CPWG Line Model

Unlike the coaxial line structure, which was divided into 30 slices, the CPWG line structure was divided into three slices. The great reduction in number is slices is due to the relatively

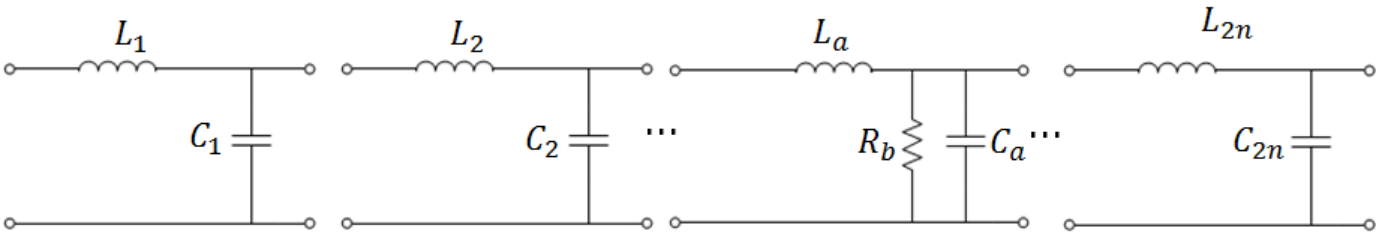

Fig. IV.7. Example of the cascaded full circuit

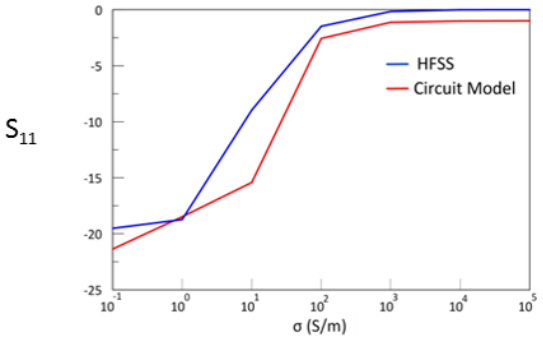

Fig. IV.8. S_{11} Comparison

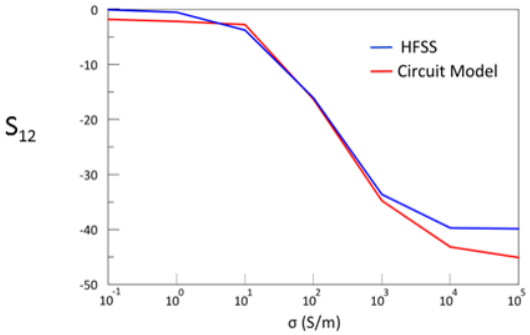

Fig. IV.9. S_{12} Comparison

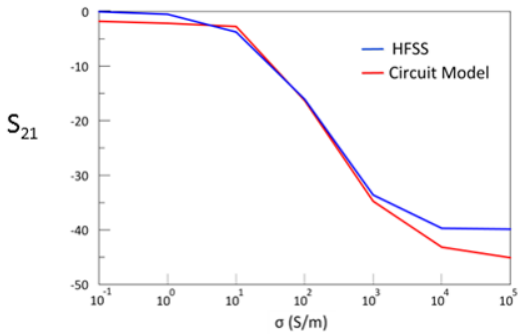

Fig. IV.10. S_{21} Comparison

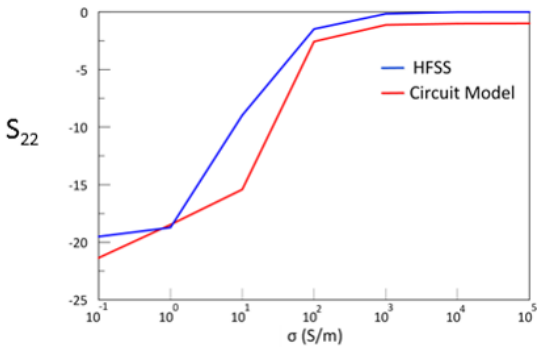

Fig. IV.11. S_{22} Comparison

few changes in geometry in the CPWG line structures that result in a change in Z_0 or γ. Like with the coaxial structure, for any lossless portion of transmission line, we modeled the particle-less slices as $L - C$ circuits. The L and C were found using equation IV.8. In the CPWG design, there were two lossless slices of equal geometry with L = 9.89 μH and C = 3.95 nF. For the $\sigma = 0$ case, the center portion was also considered a lossless section of transmission line. For this case, the L = 14.1 μH and C = 128 pF. When the particles are activated, the slice becomes a lossy section of transmission line. The lossy portions of the CPWG design were modeled as an $L - R - C$ network. The L and C are the same as the $\sigma = 0$ case calculated earlier. Like the coaxial line model, the R value was calculated using equation IV.7 and calculated as a function of σ. The results for the R vs σ can be seen in Fig. IV.12. After determining values values for L, C, and R, we calculated Z_0 and γ for

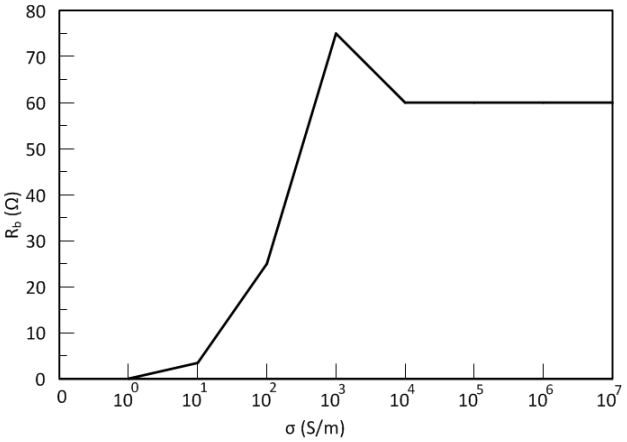

Fig. IV.12. R_b as a function gap conductivity

each slice using Fig. IV.8 and Fig. IV.9. We then found the appropriate ABCD matrix for each slice and multiplied the matrices together to determine the ABCD matrix for my full model. We then repeated this procedure for all values of σ, and obtained S-parameters as shown in Fig. IV.13, Fig. IV.14, Fig. IV.15, and Fig. IV.16. The equivalent circuit model curves closely approximate the simulate results, confirming that the equivalent circuit model for a CPWG line properly characterizes the previously simulated structure.

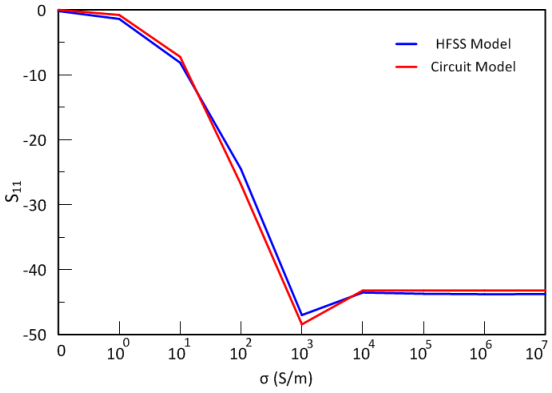

Fig. IV.13. S_{11} Comparison

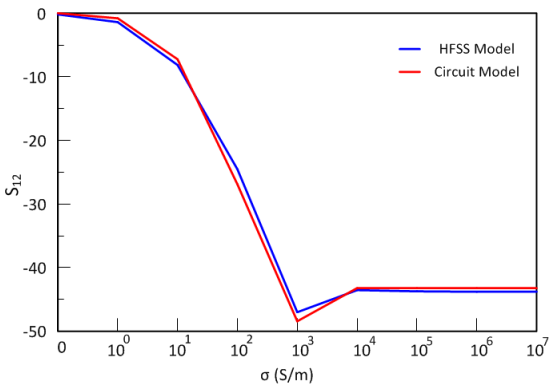

Fig. IV.14. S_{12} Comparison

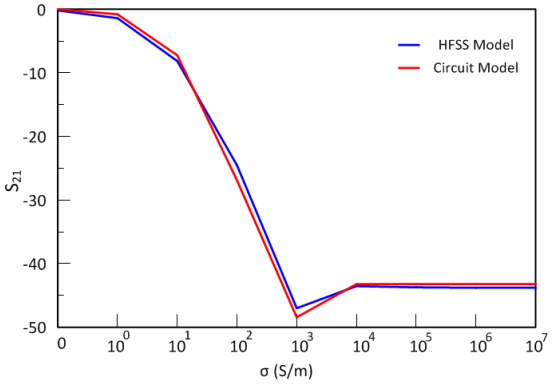

Fig. IV.15. S_{21} Comparison

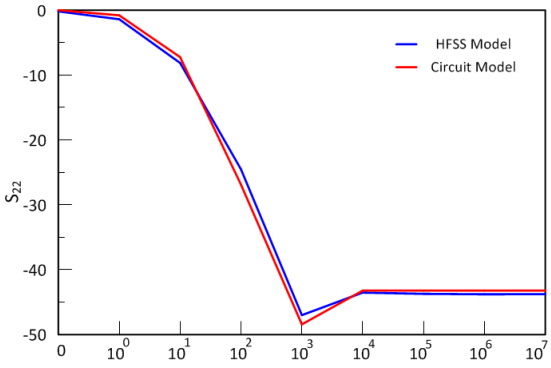

Fig. IV.16. S_{22} Comparison

Conclusion and Future Work

In this work, we have used the colloidal microstructures characterized in [1] to develop filtering devices. The devices analyzed in simulation obtained over 30 dB of attenuation at 3 GHz for both the coaxial line based and CPWG line based structures. In addition, we developed equivalent circuit models for both types of devices to characterize the function of the colloidal microstructures within the transmission line structures. Now that we have structures simulated and analyzed, the future work focuses on fabrication and testing of the devices. In the immediate future, we plan to perform RF measurements on the fabricated two dimensional structures and begin developing methods for fabricating a three dimensional coaxial structure. In addition, we plan to further explore the equivalent circuit model, particularly by analyzing the circuit performance in relationship to particle shape, size, and orientation. We hope this project continues on to develop fully deployable reconfigurable filtering devices for HPTW mitigation and further explore the use of colloidal microstructures in RF systems.

REFERENCES

[1] Pradipkumar Bahukudumbi, Neil W.Everett, Ali Beskok, Michael A. Bevan, Gregory H.Huff, Dimitris Lagoudas, and Zoubeida Ounaies. "colloidal microstructures, transport, and impedance properties within interfacial microelectrodes". *Applied Physics Letters*, 90(22), 2007.

[2] G. Champiot. *Electromagnetic compatibility (EMC) Part 2: Environment Section 9: Description of HEMP environment - Radiated disturbance.* IEC, 1996.

[3] K. Change. *RF and Microwave Wireless Systems.* Jon Wiley and Sons Inc, 2000.

[4] F. Christophe, R. Klein, X. Ferrieres, and S. Bolioli. Distributed microwave breakdown for shielding of sensitive electronics against frontdoor overloads. In *Plasma Science (ICOPS), 2011 Abstracts IEEE International Conference on*, pages 1–1, 2011.

[5] M.H. Nagrail and A. Hellany. Radiated and conducted emi emissions in switch mode power supplies (smps): sources, causes and predictions. 2001.

[6] W Radasky. High-altitude electromagnetic pulse (hemp): A threat to our way of life. *Today's Engineer*, 2007.

[7] A. Sihvola. *Electromagnetic Mixing Formulae and Applications.* IET, 2000.

[8] P.S. Winokur. Why semiconductors must be hardened for space deployment. *NPSS Newsletter*, 2000.